Quantitative Reconstruction of Dielectric Properties Based on Deep-Learning-Enabled Microwave-Induced Thermoacoustic Tomography

Zhaoxu Luo, Chenzhe Li, *Graduate Student Member, IEEE*, Dantong Liu, Baosheng Wang, *Student Member, IEEE*, Lejia Zhang, Yuexin Ma, Kuiwen Xu, *Member, IEEE*, and Xiong Wang, *Member, IEEE*

***Abstract*— Quantitative reconstruction of dielectric properties has enabled a wealth of biomedical applications. Although traditional microwave imaging and microwave-induced thermoacoustic tomography (MITAT) techniques have been widely explored for quantitative reconstruction, it is still highly challenging for them to deal with biological samples with high permittivity and conductivity. This work leverages deep-learning-enabled MITAT (DL-MITAT) approach to quantitatively reconstruct dielectric properties of biological samples with high quality. We construct a new network structure to separately reconstruct the permittivity and conductivity. By simulation and experimental testing, we demonstrate that the DL-MITAT technique is able to reliably reconstruct inhomogeneous biological samples with tumor, muscle, and fat. The experimental reconstruction error is only 5%. The network exhibits excellent generalization capability in terms of sample's geometry. This work provides a useful paradigm and alternative way for quantitative reconstruction of dielectric properties and paves the way toward practical applications.**

***Index Terms*— Deep learning (DL), dielectric property reconstruction, microwave imaging, microwave-induced thermoacoustic tomography (MITAT), quantitative reconstruction.**

I. Introduction

QUANTITATIVE reconstruction of the dielectric properties of samples via electromagnetic imaging techniques is of paramount significance for a plethora of disciplines [1], [2], [3], [4], [5], [6], [7], [8], [9], [10], [11], [12], [13], [14], among which the biomedical applications have attracted tremendous attention and research activities. Breast cancer diagnosis is the most extensively explored area [6], [7], [8], [9], [10], which is enabled by the obvious dielectric contrast between malignant and healthy tissues. Similarly, the detection of brain tumor and brain hemorrhage have also been demonstrated [11], [12]. Because the dielectric property of blood is dependent on the concentration of glucose, it is possible to noninvasively determine the blood glucose level by microwave detection techniques [13]. Microwave imaging can also be employed to quantitatively retrieve dielectric property of biological tissue, such as bone health evaluation [14], leg imaging [15], breast tumor detection [16], and head imaging [17].

Microwave imaging technology has been well developed to accurately and quantitatively reconstruct the constitutive parameters, i.e., both the permittivity and conductivity distribution of the samples via the inverse scattering-based inversion methods [15], [16], [17], [19]. However, inverse scattering-based inversion methods encounter some challenges owing to the intrinsic ill-posedness and nonlinearity. The nonlinearity with respect to the unknown constitutive parameters is due to multiple scattering effects inside the domain of interest. When dealing with strong scatterers (those with high dielectric contrasts against the background and/or electrically large dimensions), multiple scattering effects are significantly remarkable and the corresponding nonlinearity is increased remarkably. Consequently, one major drawback of the current quantitative microwave imaging techniques is that samples bearing high permittivity and contrast (e.g., skins, breast glandular tissues, muscles, and tumors) are challenging to be faithfully reconstructed due to high nonlinearity [20], [21], [22], [23], [24], [25], [26], [27]. This issue inhibits many potential applications of the quantitative inversion via microwave imaging.

Microwave-induced thermoacoustic tomography (MITAT) has exhibited intriguing advantages for biomedical applications, such as cancer detection [6], [7], [8], brain hemorrhage imaging [12], [29], foreign object detection [30], surgery guidance [31], and so on. MITAT essentially leverages the dielectric contrast in a biological sample and recovers an image, referred to as thermoacoustic (TA) image, of the sample's microwave power absorption distribution [32], [33]. MITAT can also be applied to quantitatively reconstruct

Manuscript received 8 November 2022; revised 29 November 2022; accepted 7 December 2022. Date of publication 2 March 2023; date of current version 5 June 2023. This work was supported in part by the National Natural Science Foundation of China under Grant 61971287, in part by the Open Project of State Key Laboratory of Millimeter Waves under Grant K202207, and in part by the Double First-Class Initiative Fund of ShanghaiTech University under Grant SYLDX035 2022. *(Corresponding authors: Kuiwen Xu; Xiong Wang.)*

Zhaoxu Luo, Chenzhe Li, Baosheng Wang, Lejia Zhang, Yuexin Ma, and Xiong Wang are with the School of Information Science and Technology, ShanghaiTech University, Shanghai 201210, China (e-mail: wangxiong@shanghaitech.edu.cn).

Dantong Liu is with the School of Life Science and Technology, ShanghaiTech University, Shanghai 201210, China.

Kuiwen Xu is with the Engineering Research Center of Smart Microsensors and Microsystems, Ministry of Education, Hangzhou Dianzi University, Hangzhou 310018, China (e-mail: kuiwenxu@hdu.edu.cn).

Color versions of one or more figures in this article are available at https://doi.org/10.1109/TMTT.2023.3234466.

Digital Object Identifier 10.1109/TMTT.2023.3234466

permittivity and conductivity distributions in a sample [2], [3], [4], which are directly related to the power absorption distribution [34]. However, the quality and accuracy of the reconstructed dielectric property still need to be improved, especially for inhomogeneous biological samples [35]. In addition, the previous works demand the permittivity distribution as a priori knowledge (only the conductivity can be recovered), which is not practical in reality.

Deep learning (DL) has been extensively applied in diversified disciplines in science and engineering in the past five years [36], [37]. This work investigates a DL-enabled MITAT (DL-MITAT) approach to perform high-quality quantitative reconstruction of dielectric properties. The contribution of the work could be summarized as follows.

1) A new network structure called double-branch residual U-Net (DBResU-Net) is proposed to implement the DL-MITAT. Quantitative reconstruction of the dielectric properties of some heterogeneous biological samples with fat, muscle, and tumor is used to evaluate the proposed technique. We carry out both microwave and acoustic simulations to efficiently establish the training sets. The physical transformation is implemented via the back-projection (BP) algorithm from collected acoustic signal data to the preliminary TA image or distribution information, which is taken as the input of the network.
2) The proposed DBResU-Net is composed of a cascaded coarse network and a fine-tuning model to fulfill the high-quality imaging from the preliminary results of the BP to the output of permittivity and conductivity. This can significantly improve the reconstruction accuracy compared to traditional MITAT methods. The two branches in the fine-tuning model can separately yield outputs of the permittivity and conductivity, which is beyond the capability of traditional MITAT techniques.
3) Simulation testing results reveal reliable quantitative reconstruction, even if when handling testing samples with shapes different from those in the training sets. The presented experimental results based on some fabricated inhomogeneous phantoms demonstrate that this method is able to obtain high-quality reconstruction results and less than 5% error in the value of the dielectric properties. Experimental testing results using mismatched samples are also discussed.

Compared to our previous work on DL-MITAT [9], this work is fundamentally different in terms of four aspects. First, this work conducts quantitative reconstruction that is much more challenging than the qualitative reconstruction in [9]. Second, to achieve quantitative inversion of complex permittivity, there is a big distinction between the utilized network structures. The network in [9] is a domain transform network that uses original data as the input and finally gets an output image. In contrast, the current network does not need to do physical domain transfer, i.e., both the input and output of the network are the physically constitutive images. In addition, the current network has a double-branch structure to yield two output images and the loss function is dependent on both the output images. Third, building the training sets in this work involves both microwave and acoustic simulations, while only acoustic simulation is needed in [9]. This can largely guarantee the accuracy of the quantitative reconstruction in this work, especially for complicated biological samples. Fourth, Zhang et al. [9] mainly investigate the image reconstruction using sparse data, while the current work uses complete data. Last but not least, Zhang et al. [9] only investigate the detection of a simple target, i.e., a round breast tumor. However, the current work deals with a much more difficult task to reconstruct the 2-D dielectric property distribution maps of complicated inhomogeneous samples.

This work provides an alternative way for quantitative reconstruction of biological samples' dielectric properties and is meaningful for many related biomedical detection and imaging applications.

II. Rationale

A. Fundamentals of MITAT

The well-established MITAT theorem suggests that time-domain TA pressure signals $p(\vec{r},t)$ can be described as [32], [38], [39], [40]

$$p\left(\vec{r},t\right)=\frac{\beta\rho}{4\pi C_p}\iiint\limits_{U_0}\frac{1}{\left|\vec{r}-\vec{r}_0\right|}\left[\frac{\partial S\left(\vec{r},t\right)}{\partial t}\right]_{t=t-\frac{\left|\vec{r}-\vec{r}_0\right|}{c}}d\vec{r}_0$$
$$=\frac{\beta\rho}{4\pi C_p}\iiint\limits_{U_0}\frac{A\left(\vec{r}\right)}{\left|\vec{r}-\vec{r}_0\right|}\left[\frac{\partial I(t)}{\partial t}\right]_{t=t-\frac{\left|\vec{r}-\vec{r}_0\right|}{c}}d\vec{r}_0 \quad (1)$$

where $S(\vec{r},t)=\sigma(\vec{r})|\vec{E}(\vec{r},t)|^2/2\rho(\vec{r})=A(\vec{r})I(t)$ represents the specific absorption rate (SAR) [34], U_0 is the spatial region, in which SAR or $A(\vec{r})$ is nonzero, $\vec{r}_0$ is an arbitrary spatial location in U_0, β (K^{-1}) denotes the thermal expansion coefficient, ρ ($\mathrm{kg}\cdot\mathrm{m}^{-3}$) denotes the mass density, C_p ($\mathrm{J}\cdot\mathrm{K}^{-1}\cdot\mathrm{kg}^{-1}$) denotes the specific heat capacity, c ($\mathrm{m}\cdot\mathrm{s}^{-1}$) denotes the speed of sound, and σ ($\mathrm{S}\cdot\mathrm{m}^{-1}$) denotes the conductivity.

In practical MITAT systems, the time-domain acoustic pressure signal $p(\vec{r},t)$ stemming from a sample is received by ultrasound transducers at different locations $\vec{r}$. The BP algorithm aims to inverse (1) from the measured $p(\vec{r},t)$ and reconstruct $A(\vec{r})$, which reveals the spatial distribution of SAR and is referred to as a TA image. If all the transducers are located on a sphere, $A(\vec{r})$ can be solved as [32]

$$A(\vec{r})=-\frac{r^2C_p}{2\pi c^4\beta}\iint\limits_{W}dW\frac{1}{t}\frac{\partial p(\vec{r},t)}{\partial t}\Big|_{t=\frac{\left|\vec{r}_0-\vec{r}\right|}{c}} \quad (2)$$

where r is the radius of the scanning sphere and W represents the spherical surface, on which $p(\vec{r},t)$ is recorded.

As suggested by (1) and the definition of $S(\vec{r},t)$, the recovered TA image $A(\vec{r})$ directly contains the distribution information of σ. As suggested by Maxwell's equations $\nabla\times\vec{E}=-j\omega\mu\vec{H}$ and $\nabla\times\vec{H}=j\omega(\varepsilon-j\sigma/\omega)\vec{E}$, the electric field $\vec{E}$ in a sample is dependent on both ε and σ, which

means that $A(\vec{r})$ can reveal information of the distribution of both ε and σ. Due to the complexity of electromagnetic wave propagation and attenuation in an inhomogeneous sample, the relationship between $A(\vec{r})$ and ε and σ is an implicit function. This implies that ε and σ cannot be extracted from $A(\vec{r})$ via a simple explicit way. Accordingly, we take advantage of DL to quantitatively reconstruct ε and σ.

As seen from (1), the generated TA signal $p(\vec{r}, t)$ is proportional to $S(\vec{r}, t)$. Thus, for biological samples with roughly the same mass density, the higher the loss or conductivity, the stronger the generated TA signal signal-to-noise ratio (SNR) from the sample [7]. For samples bearing weak microwave losses that generate TA signals with low SNR, they are likely to be missed or exhibit low quality in the reconstructed image. Thus, the proposed DL-MITAT technique for quantitative reconstruction of dielectric properties is suitable for high-loss samples rather than low-loss or lossless samples.

B. Structure of Applied Network

U-Net, based on fully convolutional network, is one of the most widely used DL models in the field of biomedical imaging [41]. Its architecture can be considered as a contracting path (or an encoder network) to encode the input image into feature representations and a symmetric expansion path (or a decoder network) to semantically project the features learned by the encoder into pixel space to get precise localization. Compared to the traditional U-Net, the residual U-Net (ResU-Net) establishes a skip connection to add the input data to the output data, which makes the network converge faster and more robust [42]. ResU-Net has been proven to be effective in medical imaging [43], [44] and image segmentation [45].

In this work, we modify the ResU-Net into DBResU-Net to better fit the current problem of reconstructing both of permittivity and conductivity, which is quite different from that used in [9]. The architecture of DBResU-Net is shown in Fig. 1. It consists of a coarse model and a fine-tuning model. Different from the traditional ResU-Net, after the last encoder layer, we split the network into two branches in order to separately convolute the features into two outputs. The coarse model is shown in Fig. 1(a), which learns general features of the input image. The two branches after it form the fine-tuning model, as shown in Fig. 1(b). It projects the features extracted by the coarse model into two different spaces to get two outputs, namely, the permittivity and conductivity. Since both the permittivity and conductivity are reconstructed from the TA image, we first take the coarse model to extract the common features shared by both the permittivity and conductivity. In light of the fact that the permittivity and conductivity distributions are usually different from each other, the double branches in the fine-tuning model are suitable for separately reconstruct the features of these two dielectric properties.

C. Framework of DL-MITAT Reconstruction Method

The framework of the DL-MITAT technique for reconstructing the permittivity and conductivity is shown in Fig. 2. It mainly contains three sections, i.e., data construction, training, and testing.

In this work, we construct the training sets via microwave and acoustic simulations, which is much more time-efficient and cost-effective than using experimental approaches [46]. We apply CST microwave studio software to perform microwave simulations to get the SAR in the sample. The dielectric property distributions serve as the ground truth (GT) data. We subsequently utilize the k-Wave MATLAB Toolbox [47] to carry out the TA simulations based on the obtained SAR to acquire the acoustic signals detected by transducers. The obtained acoustic signals are used to get an image by the conventional BP algorithm, which is applied as the input data of the DBResU-Net. The input data exhibit SAR distribution in the sample, and using such an input data can be considered as embedding the physics of MITAT into the DL-MITAT technique to improve the performance. It should be noted that the previous DL-MITAT work [9] uses approximate SAR distribution in the acoustic simulations for the data construction, i.e., no microwave simulation is needed. This way is acceptable for the relatively simpler target in [9] (a round tumor in fatty tissue), but not suitable for the current work that deals with a complicated inhomogeneous biological sample. Thus, we take the CST software to obtain the accurate SAR in the sample to enhance the accuracy of the quantitative reconstruction at the cost of more computation time.

Detailed procedure of the data construction is shown in Fig. 2(a) and described as follows.

Step 1: We first need to configure the CST numerical microwave simulation. The setup of the CST simulation is similar to the corresponding practical experimental environment. Two dielectric parameters including permittivity and conductivity as well as one acoustic parameter, mass density, are needed in the simulations, each of which is set to be a 3-D distribution map with a size of $D_x \times D_y \times D_z$. The sample has a size of $C_x \times C_y \times C_z$, which is smaller than $D_x \times D_y \times D_z$. We construct N_t different samples by varying some parameters to do N_t sets of CST simulations. Detailed parameters for different samples are described in Section III.

Step 2: We then conduct N_t sets k-Wave simulations. To speed up the simulations, we simplify the problems to 2-D, which means that both the sample and simulation environment are 2-D. The initial pressure map (proportional to SAR) with a size of $C_x \times C_y$ is calculated. We set the microwave pulse the same as that to be utilized in experiments. Two acoustic parameters including the speed of sound and mass density are needed in the simulations, each of which is set to be a 2-D distribution map with a size of $D_x \times D_y$. We deploy an M-element circular transducer array enclosing the sample to receive the generated acoustic signals. The simulation results are time-domain TA signals with a size of $M \times L \times N_t$, with L denoting the number of time points. It should be noted that the $D_x \times D_y$ domain can be theoretically set to a nonrectangular shape, e.g., a circle just enclosing the transducer array, but setting an overall circular simulation domain in CST and k-Wave is not convenient.

Step 3: We filter the simulated time-domain acoustic signals by the properties of realistic transducers. We add white

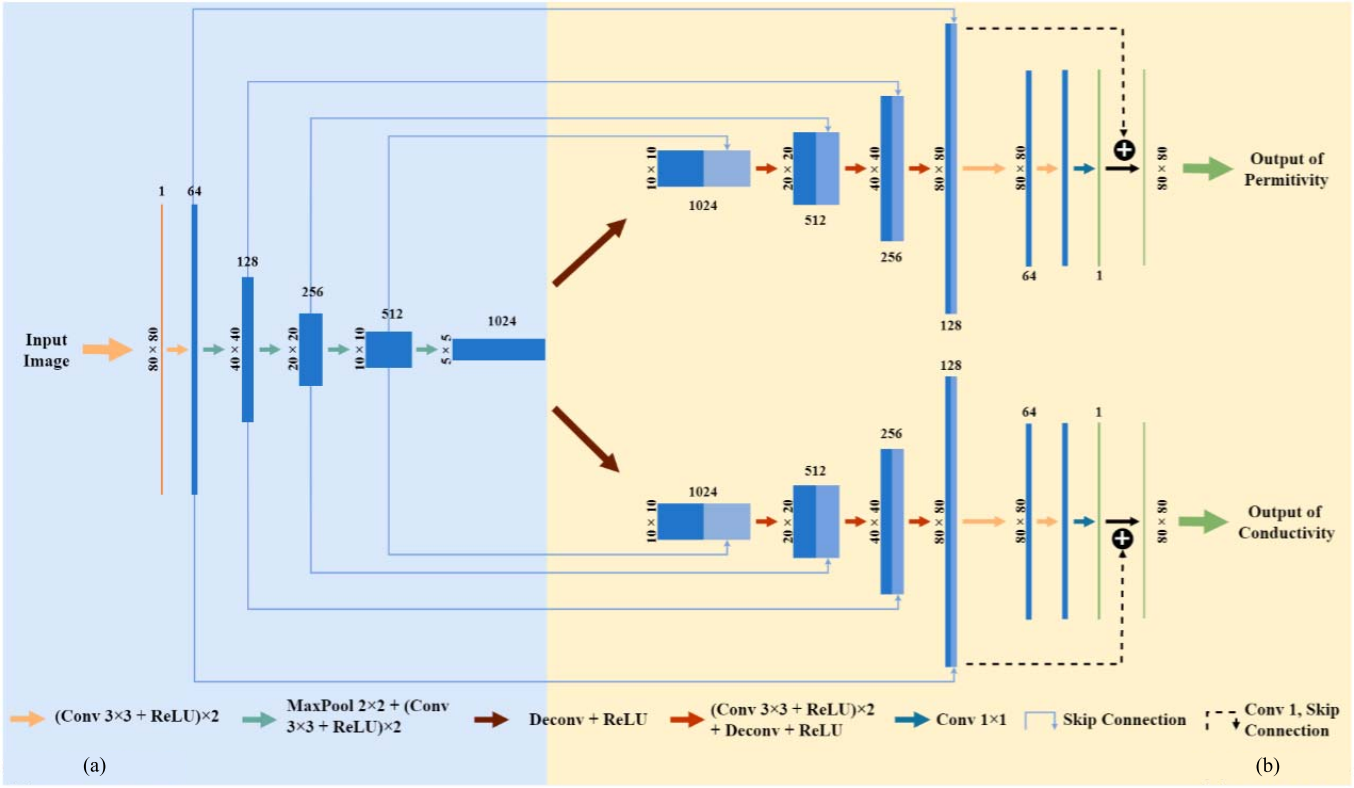

Fig. 1. Structure of the proposed DBResU-Net. (a) Coarse model. (b) Fine model.

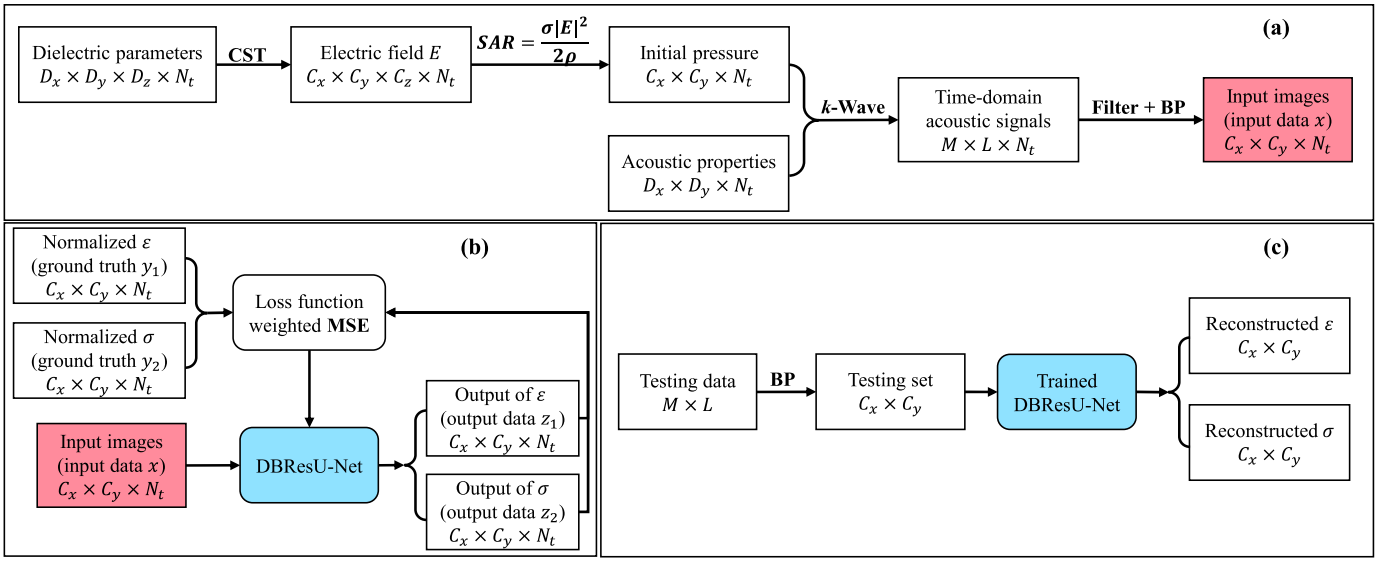

Fig. 2. Framework of the entire procedure of the proposed DBResU-Net-based DL-MITAT technique for the reconstruction of permittivity and conductivity. (a) Data construction section. (b) Training section. (c) Testing section.

Gaussian noise to the signals to improve the similarity between the simulated and experimental signals. We apply the conventional BP algorithm to reconstruct N_t images (size of $C_x \times C_y$) of the sample based on a homogeneous lossless acoustic environment.

The training phase is given in Fig. 2(b). The BP images are treated as the input data to the DL network. By this manner, the physics of the MITAT framework is automatically embedded into the network. The GT data are the corresponding permittivity and conductivity of the sample with a size of $C_x \times C_y$, which is the same as the dielectric parameter of the sample used in the CST simulations. We train the network by iteratively minimizing the loss function given by

$$\text{Loss} = \alpha \text{mse}(y_1, z_1) + \beta \text{mse}(y_2, z_2) \tag{3}$$

$$\text{mse}(y_i, z_i) = \frac{1}{B} \sum_{l=1}^{B} \left(y_i^{(l)} - z_i^{(l)} \right)^2 \tag{4}$$

where $y_i^{(l)}$ and $z_i^{(l)}$, respectively, denote the GT data and the output data, with $i = 1$ for permittivity and $i = 2$ for conductivity. l denotes the lth data and B denotes the batch size for each training. α and β are, respectively, the weights

TABLE I
SETUP OF NETWORK TRAINING

Parameter	Value/Type
Batch size	50
Epoch	200
Initial Learning Rate	1e-4
Optimizer	Adam
Learning Rate Schedular	StepLR

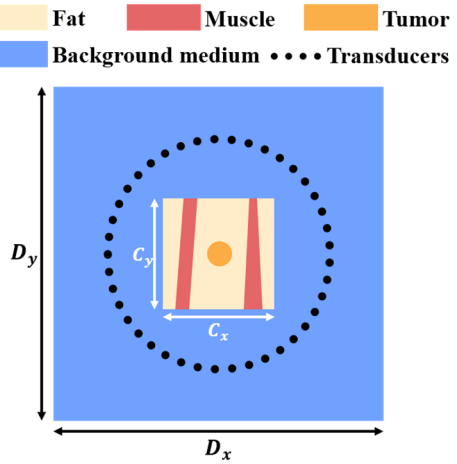

Fig. 3. Schematic of the inhomogeneous breast phantom.

of mse error for permittivity and conductivity. The setup of the training is given in Table I [48]. We employ PyTorch framework to do the network training on a PC with a NVIDIA RTX A6000 GPU card. During the training process, the parameters in the DBResU-Net are iteratively optimized. With sufficient training of the network, the output will be in high agreement with the GT data. We name the final version as a trained DBResU-Net and its output as the reconstructed permittivity and conductivity.

In the testing phase shown in Fig. 2(c), the testing data refer to the time-domain TA pressure signals obtained by either simulation or experiment, which has a size of $M \times L$. We then perform BP algorithm to obtain a testing set image with a size of $C_x \times C_y$ and feed this image to the trained network. Finally, we obtain the reconstructed permittivity and conductivity map with a size of $C_x \times C_y$.

III. TESTING BY SIMULATIONS

A. Construction of Training Sets

To verify the performance of our proposed DBResU-Net-based DL-MITAT method for quantitative reconstruction of permittivity and conductivity, we first perform simulation testing using a breast phantom. The main advantage of simulation is that the GT of permittivity and conductivity is exactly known and reconstruction errors can be accurately calculated. The schematic of the 2-D breast phantom is displayed in Fig. 3, which is a square-shaped inhomogeneous phantom composed of fat, muscle, and tumor. The breast phantom is immersed in a background acoustic coupling liquid with a speed of sound of 1460 m/s and a density of 960 kg/m^3. Dimensions of the entire

TABLE II
ACOUSTIC PARAMETERS OF THE SAMPLE

Material	Density (kg/m^3)	Speed of sound (m/s)
Fat	930	1440
Muscle	1040	1570
Tumor	1040	1570

TABLE III
DIELECTRIC PARAMETERS OF THE SAMPLE

Material	Permittivity	Conductivity (S/m)
Fat	7	0.17
Muscle	49-57	2.1-2.5
Tumor	73	2.7

k-Wave simulation region and imaging region are, respectively, set to be 280 × 280 pixels ($D_x = D_y = 280$) and 80 × 80 pixels ($C_x = C_y = 80$) with a pixel size of 0.5 × 0.5 mm. In k-Wave TA simulations, in total, $M = 180$ transducers are used and located on a 63-mm-radius circle around the breast phantom.

We construct 3000 training sets with different breast phantoms, with 2700 for training and 300 for validation. Specifically, we vary the top and bottom of the trapezoidal muscle from 2 to 10 mm, the distance between the boundary of muscle and the boundary of the breast fat from 2 to 10 mm, the diameter of the tumor from 6 to 10 mm, and the location of the tumor. The acoustic and dielectric parameters used for the breast phantom in CST and k-Wave simulations are shown in Tables II and III [49]. Due to the complex composition of muscles in human breasts, the dielectric parameters of muscles have big variation ranges. Hence, in order to make our network more robust, we vary the permittivity and conductivity of muscle when constructing the training sets, where the permittivity of muscle varies from 49 to 57, and the conductivity varies from 2.1 to 2.5 S/m. The permittivity 73 and conductivity 2.7 S/m of tumor are not varied in the training sets.

In order to mimic measured signal, we add Gaussian while noises to the simulated raw signals with 20-dB SNR. This is a common manner to improve the accordance between simulated and experimental data [9]. Meanwhile, since the transducers used in practical experiments are not ideal, we filter the signals using a specifically designed filter function, which contains the frequency response characteristics of the transducers.

B. Testing Results

We train the network by using the loss function defined in (3) by setting $\alpha = \beta = 0.5$.

We compare the performance of the DBResU-Net with two other networks. One is the conventional ResU-Net (named as 2 ind. ResU-Net), where we individually train two independent ResU-Net for permittivity and conductivity, respectively. These two ResU-Net have the same structure and share the same $C_x \times C_y$ BP input images, while use different GTs (one is permittivity and the other is conductivity). The other one is also a conventional ResU-Net with the input and output channel set to be 2, one channel for permittivity and the other

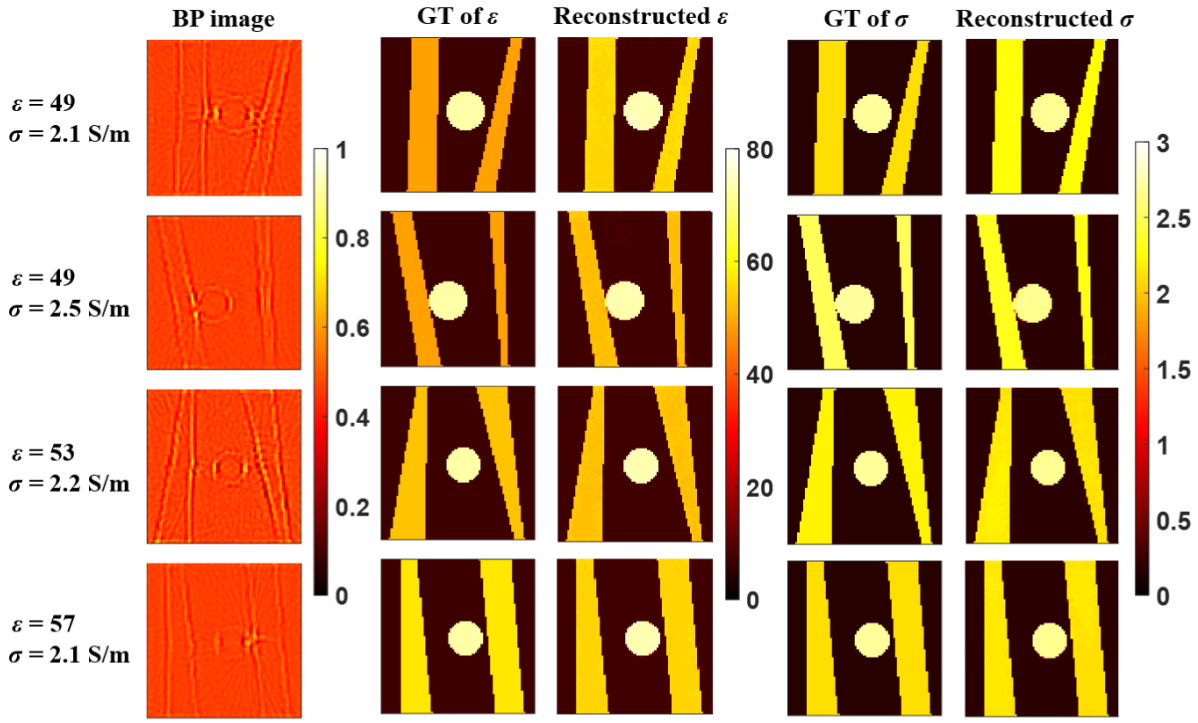

Fig. 4. Simulation testing results of phantoms with different muscle shapes and dielectric properties (labeled in the leftmost column). GT denotes the ground truth.

for conductivity. This means that both sizes of the input data and output data are $C_x \times C_y \times 2$. Similarly, the applied GT for this network also has a size of $C_x \times C_y \times 2$, with the first layer being permittivity and the second layer being conductivity.

The final reconstructed images of permittivity and conductivity are shown in Fig. 4. The GT and the images reconstructed by the conventional BP algorithm are also provided for comparison. We demonstrate the simulation results of four phantoms with different tissue dielectric properties and shapes. From the reconstructed images of the simulation results, we can see that the shapes of the muscles and tumor are reconstructed with high fidelity. The values of the permittivity and conductivity are also reliably recovered.

To quantitatively evaluate the performance of the network, we adopt the normalized percentage error (δ) defined by

$$\delta = 100\% \times \frac{1}{C_x C_y} \sum_{k=1}^{C_x} \sum_{n=1}^{C_y} \frac{|Y[k,n] - Z[k,n]|}{|Y[k,n]|} \tag{5}$$

where Y denotes the GT data, Z denotes the reconstructed data, and m and n are, respectively, the row and column indices of a pixel in the data. The mean normalized percentage errors of the 300 validation results are calculated and shown in Table IV, where δ_ε and δ_σ denote the normalized percentage errors of permittivity and conductivity, respectively. It is obvious that the designed DBResU-Net renders the lowest quantitative reconstruction error.

We then test the effect of number of training sets by using 2000 and 1000, both containing 300 for validation. It is found that the reconstruction quality declines as the number of training sets decreases. The calculated errors are tabulated in Table IV. The 3.3% and 4.1% errors of the DBResU-Net method are much better than the previous works on MITAT-based quantitative reconstruction of dielectric properties [35].

TABLE IV
NORMALIZED PERCENTAGE ERROR OF SIMULATION TESTING

Network	δ_ε	δ_σ
2 ind. ResU-Net	7.2%	8.3%
ResU-Net with 2D-output	7.3%	8.9%
DBResU-Net (3000 training sets)	3.3%	4.1%
DBResU-Net (2000 training sets)	4.2%	6.3%
DBResU-Net (1000 training sets)	8.8%	9.9%

C. Mismatch Between Training Sets and Testing Data

We then interrogate the generalization of the network applying some testing samples embracing features that are not covered by the training sets, which are also named as mismatched cases. The same training sets as those built in Section III-A are used.

First, we vary the shape of the tumor and muscles, as showcased in the first three rows in Fig. 5. It is seen that the reconstruction results are still very good even if we use an elliptical tumor and ring-shaped muscles.

Second, we further set the dielectric properties of the tumor to be higher than (the fourth row in Fig. 5) or lower than (the fifth row in Fig. 5) the ranges of those in the training sets. Although the geometries of the tumor can still be faithfully reconstructed, the values of its dielectric properties are not properly recovered. To be more specific, the reconstructed permittivity and conductivity of the tumor remain to be 75 and 2.7 S/m, respectively, for both the tested cases (the fourth and fifth rows in Fig. 5), which are almost identical to those in the training sets. Accordingly, the current network is robust in

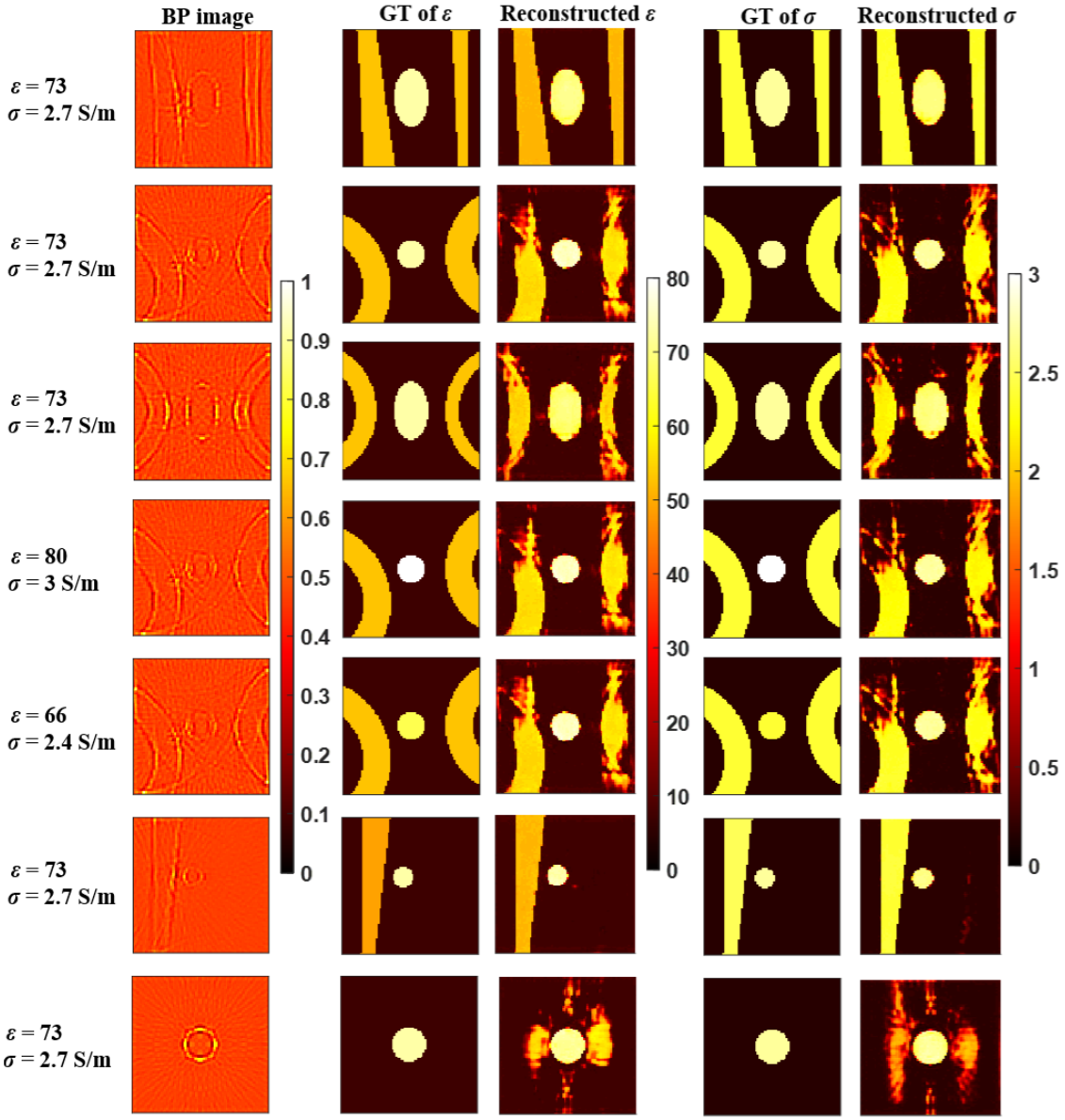

Fig. 5. Study of network generalization ability by simulations using samples with mismatched geometries or dielectric property values. The permittivity and conductivity of all muscles in this figure are, respectively, 53 and 2.4 S/m. The dielectric parameters of the tumors are labeled in the leftmost column.

dealing with mismatched geometries in the samples, whereas the proposed method roughly reconstructs the mismatched constitutive parameters of dielectric properties, in spite of some deviations. Since variation range of the dielectric properties of targeted samples in many application scenarios is known (such as biomedical imaging, foreign body detection, or nondestructive testing), this issue may not be problematic for practical applications.

Third, we interrogate a sample with only one piece of muscle (the sixth row in Fig. 5) and another sample only has a tumor (the last row in Fig. 5). The quantitative reconstruction results of the former case are still very good with negligible artifacts, but the recovered images of the latter case are marred with obvious artifacts around the tumor. Such finding is probably attributed to the fact that the latter sample has a bigger difference from the samples in the training sets than the former sample.

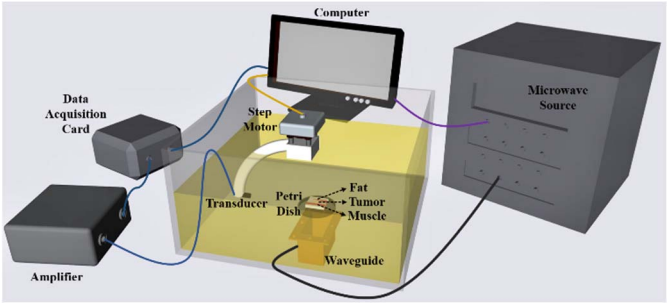

Fig. 6. Schematic of the experimental system.

IV. Testing by Ex-Vivo Experiments

A. Experimental Setup

Ex-vivo experiments are then performed to test the proposed DBResU-Net for reconstructing permittivity and conductivity.

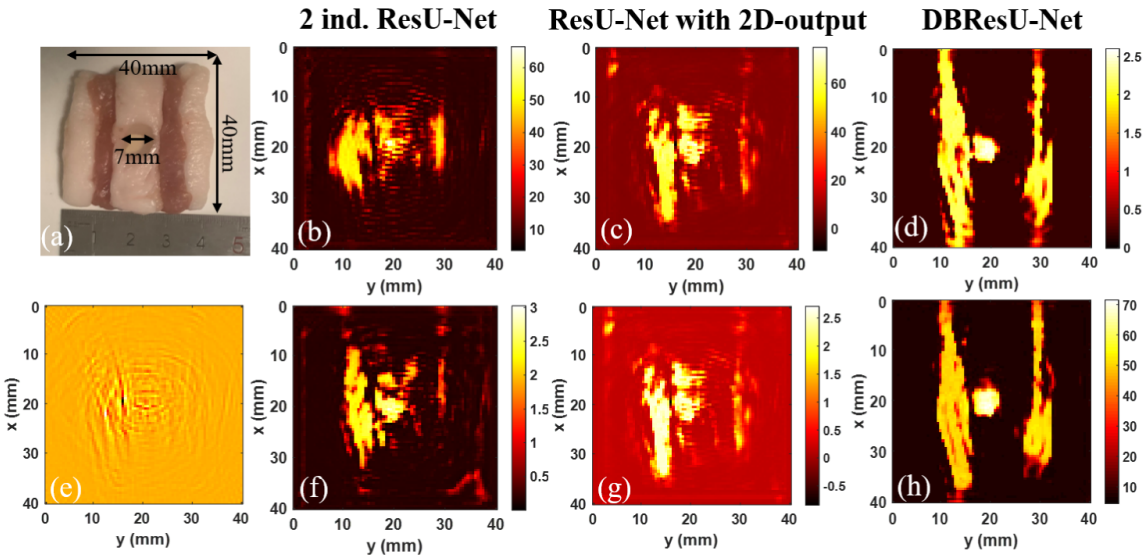

Fig. 7. Ex-vivo experimental testing results using a sample with two strip-shaped porcine muscles and a tumor phantom. (a) Photograph of the sample. (b)–(d) Permittivity reconstructed by different networks. (e) Image obtained by the BP algorithm. (f)–(h) Conductivity reconstructed by different networks.

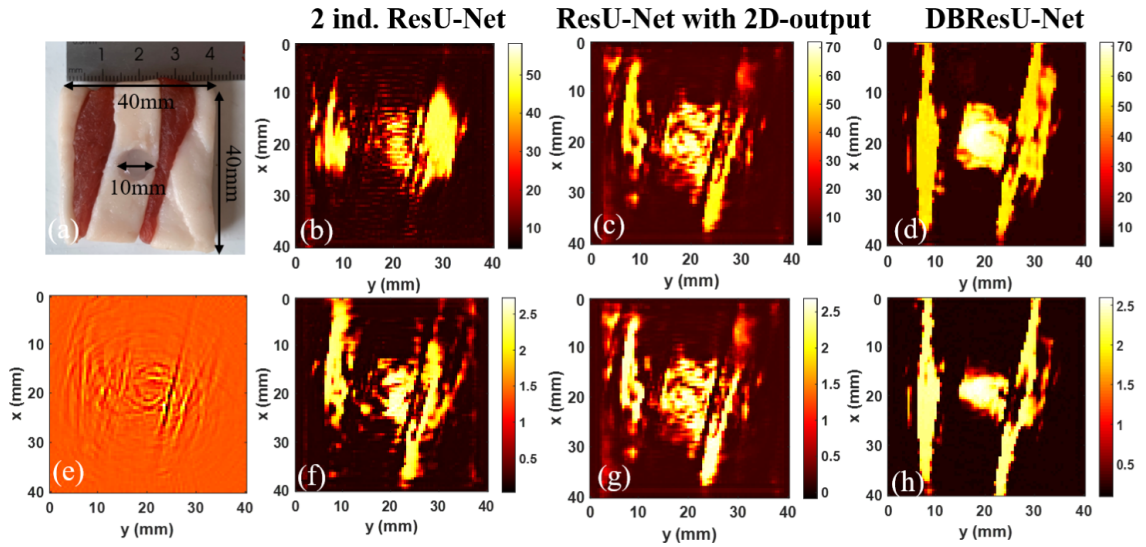

Fig. 8. Ex-vivo experimental testing results using a sample with two strip-shaped beef muscles and a tumor phantom. (a) Photograph of the sample. (b)–(d) Permittivity reconstructed by different networks. (e) Image obtained by the BP algorithm. (f)–(h) Conductivity reconstructed by different networks.

Four 40 × 40 × 8 mm inhomogeneous samples are fabricated and tested. Porcine fat, porcine muscle, beef muscle, and tumor phantoms are used in the samples. We embed a cylindrical tumor-mimicking phantom, 10 mm in diameter and 8 mm high, into each sample. The tumor-mimicking phantom is made of 83.7% deionized water, 1.2% agarose, and 15.1% salt by weight. Its permittivity and conductivity are, respectively, 73 and 2.74 S/m at 2.45 GHz, which are similar to those of the real human breast tumors [7], [10], [16]. The permittivity and conductivity of the porcine muscle at 2.45 GHz are measured by a coaxial probe (Keysight, N1501A), which are 53 and 2.2 S/m, respectively. The permittivity and conductivity of the beef muscle at 2.45 GHz are 50 and 2.5 S/m, respectively.

Schematic experimental system is shown in Fig. 6. The sample immersed in coupling liquid is radiated by a rectangular microwave waveguide antenna (WR430) beneath the tank. The antenna is fed through a coaxial cable by a microwave source pumping 2.45 GHz pulsed signals. The peak power during the microwave pulses is 20 kW.

We deploy a 2.25-MHz ultrasound transducer to measure the stimulated TA signals from the sample. The transducer is scanned around the sample at 180 discrete locations with a step of 2° and a scanning radius of 63 mm. The detected acoustic signals are subsequently amplified by a 59-dB preamplifier and recorded by a data acquisition card (PXI-5922, National Instruments) with the sampling rate of 15 MHz. Then, the signals are filtered by a bandpass filter to increase the SNR.

B. Testing Results

The training sets for the experimental testing are the same as those in Section III-A. We perform two sets of experiments by samples with two strip-shaped muscles. The sample in

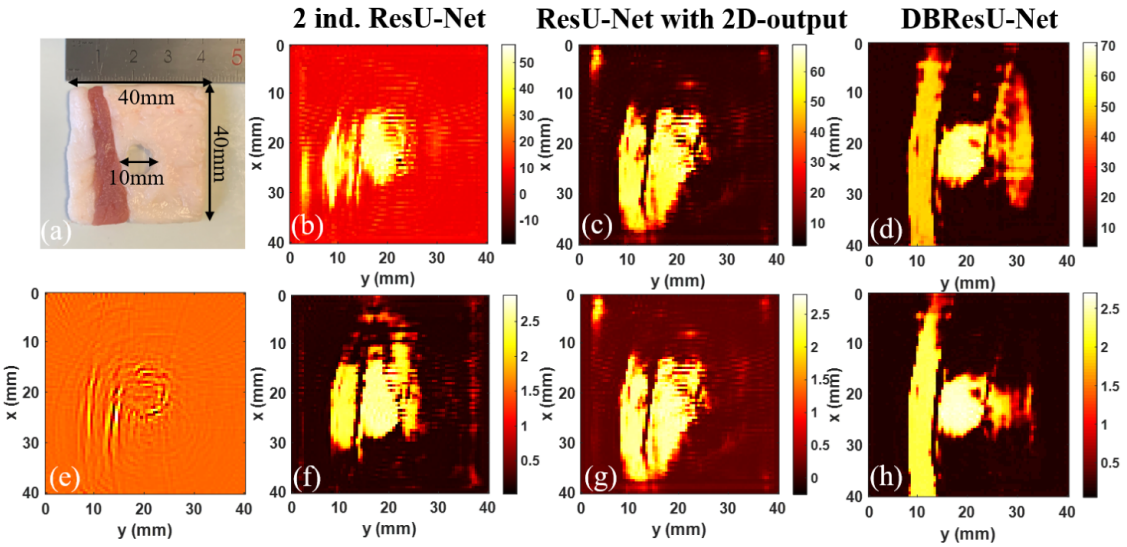

Fig. 9. Ex-vivo experimental testing results using a sample with one strip-shaped porcine muscles and a tumor phantom. (a) Photograph of the sample. (b)–(d) Permittivity reconstructed by different networks. (e) Image obtained by the BP algorithm. (f)–(h) Conductivity reconstructed by different networks.

Fig. 7(a) uses porcine muscle and the one in Fig. 8(a) uses beef muscle. Beef muscle generally has a higher conductivity while a lower permittivity compared with the porcine muscle.

The experimental testing results for the first sample are provided in Fig. 7. Compared to the other two networks, our proposed DBResU-Net can result in more accurate reconstruction in terms of both shape and value of permittivity and conductivity of the muscles and tumor. It is notable that the permittivity reconstructed by the 2 ind. ResU-Net is only 64 for the tumor-mimicking phantom, which is obviously smaller than the actual value. In contrast, the DBResU-Net can render a tumor permittivity value of 72, very close to the actual value of 73. The reconstructed permittivity of the porcine muscle is about 51 (on the left of the tumor) and 52 (on the right of the tumor), which have very good accuracy. The reconstructed conductivity of the tumor is around 2.7 S/m, showing high agreement to the actual value. The reconstructed conductivity of the muscle is 2.1 (on the left of the tumor) and 2.0 (on the right of the tumor) S/m, which almost reach the actual value of 2.2 S/m. Meanwhile, in the reconstructed images by DBResU-Net, the boundaries of different tissues are clearer than the other two networks, and the profiles of permittivity and conductivity are more continuous. For the testing results given in Fig. 8, similar performance can be observed. These experimental results undoubtedly prove that the DBResU-Net-based DL-MITAT technique can reliably reconstruct quantitative permittivity and conductivity distributions. Table V summarizes the reconstruction errors of tumor dielectric properties in this work and a previous work [35], showing the advantage of the proposed method.

It is seen that parts of the muscle near the boundary of the sample are not well recovered. This is mainly because the radiated microwave fields at these locations are not strong enough, which leads to low SNR in the generated acoustic signals and low image quality. It should also be noted that the dielectric properties of fat are recovered with lower quantitative accuracy than the muscle and tumor. This is because the fat has much lower power absorption than the muscle and tumor and generates much weaker acoustic signals, as suggested in Table III.

TABLE V
NORMALIZED PERCENTAGE ERROR OF EXPERIMENTAL TESTING

	GT of ε	Recovered ε	error	GT of σ	Recovered σ	error
This work	73	72	1.4%	2.74	2.70	1.5%
[35]	-	-	-	6.44	5.93	7.9%

C. Mismatch Between Training Sets and Testing Data

Next, we investigate two cases, where the testing data are inconsistent with the training sets in terms of shape of muscle, i.e., mismatched cases. We study two kinds of mismatches. The first sample in Fig. 9(a) has only one piece of muscle, similar to that in the sixth row in Fig. 5. The second sample in Fig. 10(a) has no muscle, similar to that the last row in Fig. 5. The applied training sets for this section remain the same as those established in Section III-A.

For the first case, the reconstructed results are showcased in Fig. 9. The obtained permittivity and conductivity profiles by the DBResU-Net still have good resemblance to the sample in Fig. 9(a), despite that the training sets and testing data are mismatched. The recovered permittivity and conductivity are, respectively, about 71 and 2.7 S/m for the tumor-mimicking phantom and 50 and 2.3 S/m for the beef muscle, implying high resemblance to the actual values. The results by the other two networks have lower accuracy in the shape and values of the muscle and tumor phantom. Meanwhile, the reconstructed image by DBResU-Net has a more accurate shape as well as boundary than the other two networks.

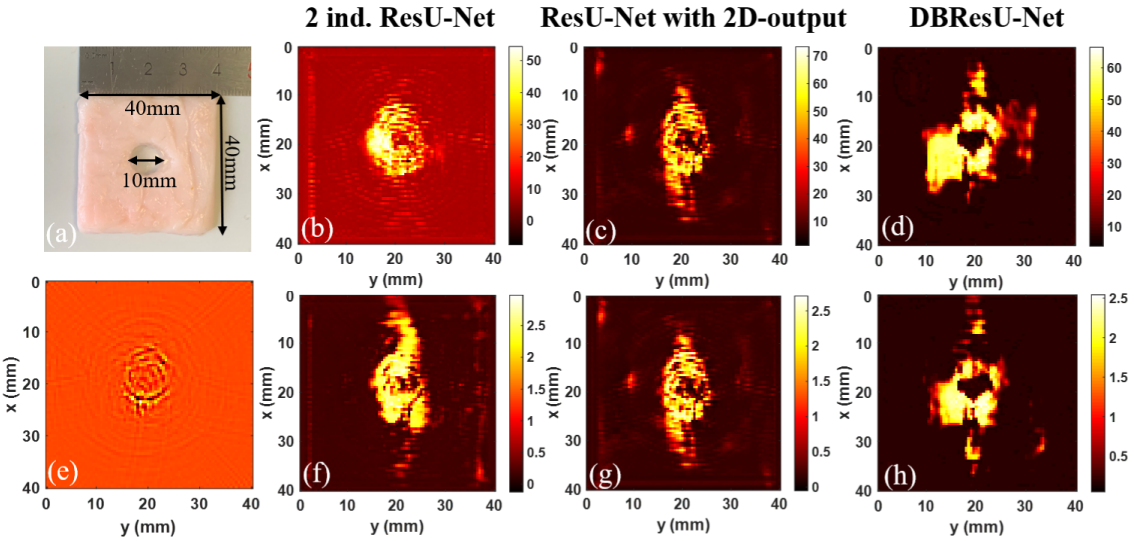

Fig. 10. Ex-vivo experimental testing results using a sample only with a tumor phantom. (a) Photograph of the sample. (b)–(d) Permittivity reconstructed by different networks. (e) Image obtained by the BP algorithm. (f)–(h) Conductivity reconstructed by different networks.

For the second case, where the sample does not have muscle, the reconstructed conductivity values by the three networks are all about 2.5 S/m for the tumor-mimicking phantom, while the reconstructed permittivity by DBResU-Net is 67, which is more accurate than that of the other two networks. However, the overall reconstruction quality is not as good as that of the first case in Fig. 9. This implies that a larger mismatch between the training sets and experimental testing data further deteriorates the quality of the reconstructed results.

D. Future Works

The DL-MITAT method for quantitative reconstruction of the permittivity and conductivity can be further improved in several aspects. First, it is interesting to employ magnetic fields to irradiate the sample, which may be capable of detecting biological tissues in a different way [50], [51]. Second, extending the applied 2-D framework to 3-D environment is very meaningful for practical applications [52]. The network needs to be revised to accommodate 3-D samples and imaging domain. It is expected that much more time and computer resources are demanded to build the training sets and train the network. Third, improving the quality of the input BP images may enhance the performance of the DL-MITAT [53]. Last, exploring new neural networks and testing the effectiveness in improving the image quality are also very meaningful [54].

V. Conclusion

This work proposes to apply the DL-based MITAT method to achieve quantitative reconstruction of biological dielectric properties. A new network called DBResU-Net composed of a coarse model and fine-tuning model is designed to implement the DL-MITAT technique. The input of the network is the preliminary TA images obtained by the physical normalization via the BP algorithm from collected acoustic waves data to the preliminary TA image or distribution information. Consequently, the proposed DBResU-Net is used to build the relationship between the preliminary TA image and the final permittivity and conductivity by the use of two branches in the output. We take advantage of numerical simulations to efficiently build the training sets. Based on the simulation testing results, it is proven the effectiveness of the proposed technique and present quantitative error analysis. Besides, it is found that this network has good generalization ability and stability when dealing with mismatched sample shapes. We further perform two experiments employing breast-mimicking biological samples. The testing results show high quality in quantitative reconstruction in terms of both shape and value of the dielectric properties, and two more samples with mismatched features from the training sets are studied. The obtained results demonstrate that the DBResU-Net is still robust in dealing with moderately mismatched cases in experiments. This work presents an alternative approach for quantitative reconstruction of dielectric properties and is meaningful for many biomedical imaging, detection, and nondestructive testing applications.

References

[1] S. Y. Semenov et al., "Microwave-tomographic imaging of the high dielectric-contrast objects using different image-reconstruction approaches," *IEEE Trans. Microw. Theory Techn.*, vol. 53, no. 7, pp. 2284–2294, Jul. 2005.

[2] L. Yao, G. Guo, and H. Jiang, "Quantitative microwave-induced thermoacoustic tomography," *Med. Phys.*, vol. 37, no. 7, pp. 3752–3759, Jul. 2010.

[3] H. Akhouayri, M. Bergounioux, A. Da Silva, P. Elbau, A. Litman, and L. Mindrinos, "Quantitative thermoacoustic tomography with microwaves sources," *J. Inverse-Posed Problems*, vol. 25, no. 6, pp. 703–717, Dec. 2017.

[4] G. Bal, K. Ren, G. Uhlmann, and T. Zhou, "Quantitative thermo-acoustics and related problems," *Inverse Problems*, vol. 27, no. 5, pp. 055007-1–055007-15, Apr. 2011.

[5] F. Caspers and J. Conway, "Measurement of power density in a lossy material by means of electro-magnetically induced acoustic signals for non-invasive determination of spatial thermal absorption in connection with pulsed hyperthermia," in *Proc. 12th Eur. Microw. Conf.*, Oct. 1982, pp. 565–568.

[6] R. A. Kruger, K. D. Miller, H. E. Reynolds, W. L. Kiser, D. R. Reinecke, and G. A. Kruger, "Breast cancer in vivo: Contrast enhancement with thermoacoustic CT at 434 MHz—Feasibility study," *Radiology*, vol. 216, no. 1, pp. 279–283, Jul. 2000.

[7] X. Wang, D. R. Bauer, R. Witte, and H. Xin, "Microwave-induced thermoacoustic imaging model for potential breast cancer detection," *IEEE Trans. Biomed. Eng.*, vol. 59, no. 10, pp. 2782–2791, Oct. 2012.

[8] L. Xu and X. Wang, "Focused microwave breast hyperthermia monitored by thermoacoustic imaging: A computational feasibility study applying realistic breast phantoms," *IEEE J. Electromagn., RF Microw. Med. Biol.*, vol. 4, no. 2, pp. 81–88, Jun. 2020.

[9] J. Zhang, C. Li, W. Jiang, Z. Wang, L. Zhang, and X. Wang, "Deep-learning-enabled microwave-induced thermoacoustic tomography based on sparse data for breast cancer detection," *IEEE Trans. Antennas Propag.*, vol. 70, no. 8, pp. 6336–6348, Aug. 2022.

[10] J. Li et al., "A preclinical system prototype for focused microwave breast hyperthermia guided by compressive thermoacoustic tomography," *IEEE Trans. Biomed. Eng.*, vol. 68, no. 7, pp. 2289–2300, Jul. 2021.

[11] S. Pereira, A. Pinto, V. Alves, and C. A. Silva, "Brain tumor segmentation using convolutional neural networks in MRI images," *IEEE Trans. Med. Imag.*, vol. 35, no. 5, pp. 1240–1251, May 2016.

[12] L. Huang, T. Li, and H. Jiang, "Thermoacoustic imaging of hemorrhagic stroke: A feasibility study with a human skull," *Med. Phys.*, vol. 44, no. 4, pp. 1494–1499, Jan. 2017.

[13] T. Yilmaz, R. Foster, and Y. Hao, "Towards accurate dielectric property retrieval of biological tissues for blood glucose monitoring," *IEEE Trans. Microw. Theory Techn.*, vol. 62, no. 12, pp. 3193–3204, Dec. 2014.

[14] P. M. Meaney, "Bone dielectric property variation as a function of mineralization at microwave frequencies," *Int. J. Biomed. Imag.*, vol. 2012, pp. 649612-1–649612-9, Jan. 2012.

[15] M. Ostadrahimi, P. Mojabi, A. Zakaria, J. LoVetri, and L. Shafai, "Enhancement of Gauss–Newton inversion method for biological tissue imaging," *IEEE Trans. Microw. Theory Techn.*, vol. 61, no. 9, pp. 3424–3434, Sep. 2013.

[16] C. Kaye, I. Jeffrey, and J. LoVetri, "Improvement of multi-frequency microwave breast imaging through frequency cycling and tissue-dependent mapping," *IEEE Trans. Antennas Propag.*, vol. 67, no. 11, pp. 7087–7096, Nov. 2019.

[17] L. Guo, N. Nguyen-Trong, A. Ai-Saffar, A. Stancombe, K. Bialkowski, and A. Abbosh, "Calibrated frequency-division distorted born iterative tomography for real-life head imaging," *IEEE Trans. Med. Imag.*, vol. 41, no. 5, pp. 1087–1103, May 2022.

[18] X. Chen, *Computational Methods for Electromagnetic Inverse Scattering*. Hoboken, NJ, USA: Wiley, 2018.

[19] Y. Zhong and X. Chen, "An FFT twofold subspace-based optimization method for solving electromagnetic inverse scattering problems," *IEEE Trans. Antennas Propag.*, vol. 59, no. 3, pp. 914–927, Mar. 2011.

[20] L. Li, H. Zheng, and F. Li, "Two-dimensional contrast source inversion method with phaseless data: TM case," *IEEE Trans. Geosci. Remote Sens.*, vol. 47, no. 6, Jun. 2009. [Online]. Available: https://ieeexplore.ieee.org/document/4695996

[21] S. Caorsi, A. Massa, M. Pastorino, and M. Donelli, "Improved microwave imaging procedure for nondestructive evaluations of two-dimensional structures," *IEEE Trans. Antennas Propag.*, vol. 52, no. 6, pp. 1386–1397, Jun. 2004.

[22] T. Isernia, L. Crocco, and M. D'Urso, "New tools and series for forward and inverse scattering problems in lossy media," *IEEE Geosci. Remote Sens. Lett.*, vol. 1, no. 4, pp. 327–331, Oct. 2004.

[23] K. Xu, Y. Zhong, and G. Wang, "A hybrid regularization technique for solving highly nonlinear inverse scattering problems," *IEEE Trans. Microw. Theory Techn.*, vol. 66, no. 1, pp. 11–21, Jan. 2018.

[24] M. Asefi, A. Baran, and J. LoVetri, "An experimental phantom study for air-based quasi-resonant microwave breast imaging," *IEEE Trans. Microw. Theory Techn.*, vol. 67, no. 9, pp. 3946–3954, Sep. 2019.

[25] M. T. Bevacqua and T. Isernia, "An effective rewriting of the inverse scattering equations via green's function decomposition," *IEEE Trans. Antennas Propag.*, vol. 69, no. 8, pp. 4883–4893, Aug. 2021.

[26] K. Xu, Y. Zhong, X. Chen, and D. Lesselier, "A fast integral equation-based method for solving electromagnetic inverse scattering problems with inhomogeneous background," *IEEE Trans. Antennas Propag.*, vol. 66, no. 8, pp. 4228–4239, Aug. 2018.

[27] K. Xu, Y. Zhong, R. Song, X. Chen, and L. Ran, "Multiplicative-regularized FFT twofold subspace-based optimization method for inverse scattering problems," *IEEE Trans. Geosci. Remote Sens.*, vol. 53, no. 2, Feb. 2015. [Online]. Available: https://ieeexplore.ieee.org/document/6842592

[28] J. C. Lin, "The microwave auditory effect," *IEEE J. Electromagn., RF, Microw. Med. Biol.*, vol. 6, no. 1, pp. 16–28, Mar. 2022.

[29] A. Yan, L. Lin, C. Liu, J. Shi, S. Na, and L. V. Wang, "Microwave-induced thermoacoustic tomography through an adult human skull," *Med. Phys.*, vol. 46, no. 4, pp. 1793–1797, Apr. 2019.

[30] Y. Sun, C. Li, B. Wang, and X. Wang, "A low-cost compressive thermoacoustic tomography system for hot and cold foreign bodies detection," *IEEE Sensors J.*, vol. 21, no. 20, pp. 23588–23596, Oct. 2021.

[31] H. Qin, Y. Cui, Z. Wu, Q. Chen, and D. Xing, "Real-time thermoacoustic imaging-guidance for breast tumor resection," *IEEE Photon. J.*, vol. 12, no. 3, pp. 1–7, Jun. 2020.

[32] B. Wang, Y. Sun, Z. Wang, and X. Wang, "Three-dimensional microwave-induced thermoacoustic imaging based on compressive sensing using an analytically constructed dictionary," *IEEE Trans. Microw. Theory Techn.*, vol. 68, no. 1, pp. 377–386, Jan. 2020.

[33] Z. Chi, X. Liang, X. Wang, L. Huang, and H. Jiang, "Detection and monitoring of osteoporosis in a rat model by thermoacoustic tomography," *IEEE J. Electromagn., RF Microw. Med. Biol.*, vol. 4, no. 4, pp. 234–239, Dec. 2020.

[34] Q. Liu, X. Liang, W. Qi, Y. Gong, H. Jiang, and L. Xi, "Biomedical microwave-induced thermoacoustic imaging," *J. Innov. Opt. Health Sci.*, vol. 15, no. 4, Jul. 2022, Art. no. 2230007.

[35] L. Huang et al., "Quantitative thermoacoustic tomography: Recovery of conductivity maps of heterogeneous media," *Appl. Phys. Lett.*, vol. 101, no. 24, pp. 244106-1–244106-3, Dec. 2012.

[36] W. Li et al., "AADS: Augmented autonomous driving simulation using data-driven algorithms," *Sci. Robot.*, vol. 4, no. 28, Mar. 2019, Art. no. eaaw0863.

[37] X. Zhu et al., "Cylindrical and asymmetrical 3D convolution networks for LiDAR segmentation," in *Proc. IEEE/CVF Conf. Comput. Vis. Pattern Recognit. (CVPR)*, Jun. 2021, pp. 9939–9948.

[38] H. Nan, S. Liu, G. J. Buckmaster, and A. Arbabian, "Beamforming microwave-induced thermoacoustic imaging for screening applications," *IEEE Trans. Microw. Theory Techn.*, vol. 67, no. 1, pp. 464–474, Jan. 2019.

[39] X. Zhu, Z. Zhao, J. Wang, J. Song, and Q. H. Liu, "Microwave-induced thermal acoustic tomography for breast tumor based on compressive sensing," *IEEE Trans. Biomed. Eng.*, vol. 60, no. 5, pp. 1298–1307, May 2013.

[40] B. Wang, Y. Sun, C. Li, Z. Wang, L. Zhang, and X. Wang, "2-D noninvasive temperature measurement of biological samples based on compressive thermoacoustic tomography," *IEEE J. Electromagn., RF Microw. Med. Biol.*, vol. 5, no. 4, pp. 371–378, Dec. 2021.

[41] O. Ronneberger, P. Fischer, and T. Brox, "U-Net: Convolutional networks for biomedical image segmentation," in *Medical Image Computing and Computer-Assisted Intervention—MICCAI 2015*. Cham, Switzerland: Springer, 2015, pp. 234–241.

[42] K. He, X. Zhang, S. Ren, and J. Sun, "Deep residual learning for image recognition," in *Proc. IEEE Conf. Comput. Vis. Pattern Recognit.*, Feb. 2016, pp. 770–778.

[43] S. Antholzer, M. Haltmeier, and J. Schwab, "Deep learning for photoacoustic tomography from sparse data," *Inverse Problems Sci. Eng.*, vol. 27, no. 7, pp. 987–1005, 2018.

[44] H. Lee, J. Lee, H. Kim, B. Cho, and S. Cho, "Deep-neural-network-based sinogram synthesis for sparse-view CT image reconstruction," *IEEE Trans. Radiat. Plasma Med. Sci.*, vol. 3, no. 2, pp. 109–119, Mar. 2019.

[45] X. Xiao, S. Lian, Z. Luo, and S. Li, "Weighted Res-UNet for high-quality retina vessel segmentation," in *Proc. 9th Int. Conf. Inf. Technol. Med. Educ. (ITME)*, Oct. 2018, pp. 327–331.

[46] T. Tong et al., "Domain transform network for photoacoustic tomography from limited-view and sparsely sampled data," *Photoacoustics*, vol. 19, Sep. 2020, Art. no. 100190.

[47] B. E. Treeby and B. T. Cox, "k-Wave: MATLAB toolbox for the simulation and reconstruction of photoacoustic wave fields," *J. Biomed. Opt.*, vol. 15, no. 2, pp. 021314-1–021314-12, 2010.

[48] D. P. Kingma and J. Ba, "Adam: A method for stochastic optimization," in *Proc. Int. Comf. Learn. Represent.*, 2015, pp. 1–15.

[49] P. A. Hasgall et al. (Feb. 2022). *IT'IS Database for Thermal and Electromagnetic Parameters of Biological Tissues*. [Online]. Available: https://itis.swiss/virtual-population/tissue-properties/overview/

[50] A. Afsari, A. M. Abbosh, and Y. Rahmat-Samii, "Modified born iterative method in medical electromagnetic tomography using magnetic field fluctuation contrast source operator," *IEEE Trans. Microw. Theory Techn.*, vol. 67, no. 1, pp. 454–463, Jan. 2019.

[51] D. Zhang et al., "Enhanced and modulated microwave-induced thermoacoustic imaging by ferromagnetic resonance," *Appl. Phys. Exp.*, vol. 12, no. 7, pp. 077001-1–077001-5, Jun. 2019.
[52] A. Afsari, A. M. Abbosh, and Y. Rahmat-Samii, "A rapid medical microwave tomography based on partial differential equations," *IEEE Trans. Antennas Propag.*, vol. 66, no. 10, pp. 5521–5535, Oct. 2018.
[53] Q. Song, Z. Wang, B. Wang, L. Zhang, and X. Wang, "Multiple back projection with impact factor algorithm based on circular scanning for microwave-induced thermoacoustic tomography," *IEEE J. Electromagn., RF, Microw. Med.*, vol. 5, no. 4, pp. 371–378, Dec. 2021.
[54] H. Zhang, Y. Chen, T. J. Cui, F. L. Teixeira, and L. Li, "Probabilistic deep learning solutions to electromagnetic inverse scattering problems using conditional renormalization group flow," *IEEE Trans. Microw. Theory Techn.*, vol. 70, no. 11, pp. 4955–4965, Nov. 2022.

Zhaoxu Luo was born in Henan, China. She is currently pursuing the bachelor's degree in electronic information engineering at ShanghaiTech University, Shanghai, China.

Her current research interests include thermoacoustic imaging and biomedical imaging based on deep learning.

Chenzhe Li (Graduate Student Member, IEEE) was born in Shanghai, China. He received the B.E. degree in electronic information engineering from ShanghaiTech University, Shanghai, in 2020, where he is currently pursuing the M.S. degree in electronic science and technology.

His current research interests include thermoacoustic imaging and biomedical imaging based on deep learning.

Dantong Liu was born in Chengdu, China. He is currently pursuing the B.E. degree at the School of Life Science and Technology, ShanghaiTech University, Shanghai, China.

He majors in biomedical engineering, and his current research interests focus on thermoacoustic imaging and biomedical imaging based on deep learning.

Baosheng Wang (Student Member, IEEE) was born in Zhejiang, China. He received the B.S. degree in automation from the China University of Petroleum, Qingdao, China, in 2016. He is currently pursuing the Ph.D. degree in electrical engineering at ShanghaiTech University, Shanghai, China.

His research interests include thermoacoustic imaging, noninvasive temperature measurement, thermoacoustic communication, and compressive sensing algorithm for biomedical imaging.

Lejia Zhang was born in Shandong, China. She received the B.E. degree in electronic information engineering from ShanghaiTech University, Shanghai, China, in 2021, where she is currently pursuing the M.S. degree in electronic science and technology.

Her research interests include thermoacoustic imaging.

Yuexin Ma received the B.Eng. degree in computer science from Shandong University, Jinan, China, in 2015, and the Ph.D. degree from the University of Hong Kong, Hong Kong, in 2019.

She is currently an Assistant Professor at ShanghaiTech University, Shanghai, China, leading the 4DV Lab. She has published more than 20 papers on top journals and conferences, including Science Robotics, TPAMI, Computer Vision and Pattern Recognition (CVPR), European Conference on Computer Vision (ECCV), The Association for the Advancement of Artificial Intelligence Conference on Artificial Intelligence (AAAI), International Joint Conferences on Artificial Intelligence (IJCAI), International Journal of Computer Vision (IJCV), ACM Transactions on Graphics (TOG), Special Interest Group on Computer Graphics and Interactive Techniques (SIGGRAPH), and so on. Her research interests lie on the computer vision and deep learning. Particularly, she is interested in 3-D perception and reconstruction.

Kuiwen Xu (Member, IEEE) received the B.E. degree from Hangzhou Dianzi University, Hangzhou, China, in 2009, and the Ph.D. degree from Zhejiang University, Hangzhou, in 2014.

From 2012 to 2013, he was a Visiting Ph.D. Student with the National University of Singapore, Singapore. From 2014 to 2015, he was a Senior Researcher with Huawei Technologies Company, Ltd., Hangzhou. He was invited to the State Key Laboratory of Terahertz and Millimeter Waves, City University of Hong Kong, Hong Kong, as a Visiting Professor, in 2018. Since September 2015, he has been with Hangzhou Dianzi University, where he is currently a Professor. He has published 50 journal articles on electromagnetics inverse problems, antenna design and synthesis, and microwave measurement and sensing. His research interests include computational imaging and electromagnetics inverse problems, machine learning-based wireless sensing and imaging, and new concept antennas (5G multiple-input multiple-output (MIMO) antenna, meta-antenna, etc.).

Xiong Wang (Member, IEEE) received the M.S. degree in electrical engineering from Clemson University, Clemson, SC, USA, in 2009, and the Ph.D. degree in electrical engineering from the University of Arizona, Tucson, AZ, USA, in 2014.

From 2014 to 2015, he was a Post-Doctoral Fellow with the University of Arizona. Since 2015, he has been with the School of Information Science and Technology, ShanghaiTech University, Shanghai, China. He has authored or coauthored more than 100 peer-reviewed journal and conference papers. His current research interests include microwave-induced thermoacoustic tomography (MITAT), thermoacoustic tomography guided cancer hyperthermia, electromagnetic and acoustic metasurfaces, deep learning for imaging, and detection applications.

Dr. Wang was a recipient of the 2012-2013 IEEE Antennas and Propagation Society Doctoral Research Award and the Shanghai Pujiang Talent Program by Shanghai Science and Technology Commission, in 2017. He is an Associate Editor of the IEEE JOURNAL OF ELECTROMAGNETICS, RF, AND MICROWAVES IN MEDICINE AND BIOLOGY and serves as the TPC Co-Chair of 2022 IEEE INTERNATIONAL MICROWAVE BIOMEDICAL CONFERENCE (IMBIOC). He is an active reviewer for *Laser & Photonics Reviews*, *Advanced Science*, IEEE REVIEWS IN BIOMEDICAL ENGINEERING, *Nano Research*, and a series of IEEE TRANSACTIONS. His graduate student has won the Best Student Paper Award of the 2019 International Conference on Microwave and Millimeter Wave Technology (ICMMT).